Draft version June 3, 2022
Typeset using LaTeX **twocolumn** style in AASTeX62

The Large Sky Area Multi-object Fiber Spectroscopic Telescope (LAMOST) Quasar Survey: Quasar Properties from Data Release Six to Nine

Jun-Jie Jin,[1,2] Xue-Bing Wu,[1,2] Yu-Ming Fu,[1,2] Xiao-Tong Feng,[1,2] Zi-Qi He,[1,2] Qin-Chun Ma,[1,2] Rui Zhu,[1,2]
Yan-xia Zhang,[3] Hai-long Yuan,[3] and Zhi-ying Huo[3]

[1] *Department of Astronomy, School of Physics, Peking University, Beijing 100871, People's Republic of China; E-mail: jjjin@pku.edu.cn; wuxb@pku.edu.cn*

[2] *Kavli Institute for Astronomy and Astrophysics, Peking University, Beijing 100871, People's Republic of China*

[3] *National Astronomical Observatories, Chinese Academy of Sciences, Beijing 100012, People's Republic of China*

ABSTRACT

We report the fourth installment in the series of the Large Sky Area Multi-Object Fiber Spectroscopic Telescope (LAMOST) Quasar Survey, which includes quasars observed between September, 2017 and June, 2021. There are in total 13,255 quasars reliably identified. Among these identified quasars, 6,385 are known ones in the SDSS DR14 quasar catalog or Million Quasars catalog, while the remaining 6,870 are newly discovered. Because LAMOST does not provide accurate absolute flux calibration, we re-calibrate the spectra with the SDSS/Pan-STARRS multi-band photometric data. The emission line properties of Hα, Hβ, Mg II and C IV, and the continuum luminosities are measured by fitting the re-calibrated spectra. We also estimate the single-epoch virial black hole masses using the derived emission line and continuum parameters. The catalog and spectra for these quasars are available online. Up to now, there are 56,364 released LAMOST quasar spectra, of which 24,312 are newly discovered. The LAMOST quasar survey not only discovers a great number of new quasars, but also provides a database for investigating spectral variability of quasars with the synergy between LAMOST and SDSS.

Keywords: catalogs - quasars: emission lines - quasars: general - surveys

1. INTRODUCTION

Quasars are a class of active galactic nuclei (AGNs), which are powered by accretion onto the supermassive black holes (SMBHs), and are the most luminous and energetic celestial objects in the universe that can emit radiation over a broad range of wavelength from radio to $\gamma-$ray (Antonucci 1993). Quasars have long been used in a variety of astrophysical studies, such as revealing the growth of SMBHs across cosmic time and the evolution connections to their host galaxies (Magorrian et al. 1998; Ferrarese & Merritt 2000; Gebhardt et al. 2000; Kormendy & Gebhardt 2001; Merritt & Ferrarese 2001; Tremaine et al. 2002), probing the distribution of interstellar and intergalactic medium (ISM and IGM), and tracing the large-scale structure of the early universe (Hennawi & Prochaska 2007; Becker et al. 2001). In addition, quasars are primary celestial references because they are distant extragalactic sources with extremely small proper motions (Feissel & Mignard 1998; Andrei et al. 2009).

Since the first discovery of the quasars in 1963 (Schmidt 1963), huge efforts have been undertaken to find more quasars. Quasars can be separated from normal galaxies and stars due to their unique features, such as the characteristic spectral energy distribution, high luminosity, variability properties and radiations at multi-wavelengths.

The most common method to select quasar candidates is based on the multi-color properties. Particularly, quasars at $z < 2.2$ have strong UV and optical emissions that distinguish them from normal stars in the color-color and color-magnitude diagrams (Fan et al. 2000; Richards et al. 2009; Schneider et al. 2007). For example, two of the most productive quasar surveys, the Sloan Digital Sky Survey (SDSS, Shen et al. 2011; Pâris et al. 2012, 2018) and the Two-Degree Fields (2dF) Quasars Redshift Survey (Boyle et al. 2000) used the optical photometric data to select quasar candidates. However, such optical color selection methods are systematically incomplete at $2.2 < z < 3.0$, especially at $z = 2.7$ as the quasars in this redshift range have similar colors to those of stellar objects (Fan 1999; Richards et al. 2002, 2006; Schneider et al. 2007). An efficient way of identifying missing quasars at $2.2 < z < 3.0$ is using the K-band photometry from the UK Infrared Telescope (UKIRT) Infrared Deep Sky Survey (UKIDSS), because quasars at $2.2 < z < 3.0$ have an excess in the near-infrared K-band when compared to stellar objects (Warren et al. 2000; Sharp et al. 2002; Lawrence et al. 2007; Maddox et al. 2008; Smail et al. 2008). Wu & Jia (2010) have demonstrated that the SDSS/UKIDSS and SDSS/WISE (Wu et al. 2012) colors can significantly improve the efficiency of quasar selection. Other main quasar candidate selection techniques based on the physical characteristics of quasars include: multi-wavelength (X-ray/radio) data matching (Schmidt 1963; Silverman et al. 2002; Carballo et al. 2004; Zeimann et al. 2011; Ai et al. 2016); variability-based selection (MacLeod et al. 2012; Ai et al. 2016); slitless-spectroscopy survey for broad emission line features (Worseck et al. 2008; Clowes 1986) and proper motion (Heintz et al. 2020).

Recently, various data-mining algorithms have also been applied to select quasar candidates, including the Kernel Density Estimation (KDE, Richards et al. 2004, 2009), the extreme deconvolution method (XDQSO, Bovy et al. 2011), support vector machine (SVM, Peng et al. 2012), Gaussian mixtrue model (Bailer-Jones et al. 2019), boosting algorithm (e.g. XGBoost, Jin et al. 2019) and deep learning (Yèche et al. 2010; Pasquet-Itam & Pasquet 2018). For example, the KDE method has been expoited in the SDSS-III Baryon Oscillation Spectroscopic survey (BOSS, Ross et al. 2012), and transfer-learning is adopted for finding quasars behind the Galactic plane (GPQs, Fu et al. 2021).

This paper presents the results of the Large Sky Area Multi-object Fiber Spectroscopic Telescope (LAMOST) Quasar Survey conducted between September, 2017 and June, 2021. This is the fourth installment in the series of LAMOST quasar survey, after data release 1 (DR1, Ai et al. 2016, hereafter Paper I), data release 2 and 3 (DR2 and DR3, Dong et al. 2018, hereafter Paper II) and data release 4 and 5 (DR 4 and DR5, Yao et al. 2019, hereafter Paper III). In this paper, the candidate selection, spectroscopic survey and quasar identification are briefly reviewed in Section 2. Spectral measurements and black hole mass estimations for new quasars are described in Section 3. The description of the quasar catalog and parameters released are presented in Section 4. At last, the summary is given in Section 5. We adopt the cosmology parameter $H_0 = 70$ km s^{-1} Mpc^{-1} and a flat universe with $\Omega_M = 0.3$ and $\Omega_\Lambda = 0.7$.

2. SURVEY OUTLINE

LAMOST, also known as Guoshoujing Telescope, is a quasi-meridian reflection Schmidt telescope with an effective aperture varies from 3.6 to 4.9m (Cui et al. 2012; Zhao et al. 2012). It is located at Xinglong Observatory, China and has a 5° (diameter) field of view. The LAMOST is equipped with 4000 fibers ($3.3''$), which are mounted on the focal plane and connected to 16 spectrographs. Each spectrum is divided into a blue channel ($3700 \sim 5900$ Å) and a red channel ($5700 \sim 9000$ Å), with an overlap of region between the two channels at 5700-5900 Å. The spectra were observed under the low-resolution mode and the spectral resolution is R $\sim$ 1000-2000 over the entire wavelength range.

After commissioning from 2009 to 2010, LAMOST began a pilot survey in 2011 (Luo et al. 2012). The LAMOST regular survey starts from September, 2012. The exposure time is adjusted according to the apparent magnitude of targets and observation conditions. The typical value of the total exposure time for a target is $\sim$ 90 minutes, which is equally divided into three sub-exposures. Although the LAMOST quasar survey used only a small fraction of the available observing time due to the limitations of LAMOST site (e.g., weather conditions, poor seeing and bright sky background), LAMOST has still collected useful data and identified more than 40,000 quasars, about half of which are new discoveries, during the first five years. This paper is the fourth installment in the series of LAMOST quasar survey.

2.1. *Target Selection*

The methods used to select the quasar candidates for LAMOST quasar survey are described in detail in Wu & Jia (2010), Wu et al. (2012), Peng et al. (2012), Paper I, II and III. Here, we give a brief description of the candidate selection.

The primary selection for quasar candidates is based on the photometric data of SDSS (Ahn et al. 2012), and the magnitudes we used here are the SDSS point-spread function (PSF) magnitudes with the Galactic extinction corrected (Schlegel et al. 1998). First, only point sources are selected to exclude galaxies. Second, the targets should be brighter than i=20 to avoid too low signal-to-noise ratio (SNR), and fainter than i=16 to avoid saturation and contamination with neighbor fibers. Various methods are then applied to further separate quasar candidates from stars. Most of the quasar candidates are selected based on the optical-infrared colors (SDSS-UKIDSS/WISE), as has been described in Wu & Jia (2010) and Wu et al. (2012). A few data-mining algorithms are also used to selected quasar candidates, such as SVM classifiers (Peng et al. 2012), extreme deconvolution method (XDQSO, Bovy et al. 2011), and KDE (Richards et al. 2009). In addition, some quasar candidates are selected by cross-matching SDSS photometry with the detected sources in X-ray surveys (XMM-

Newton, Chandra, ROSAT) and radio surveys (FIRST, NVSS).

Although some of the selected candidates have already been identified by SDSS after our target selections, we include them in the LAMOST survey, which will be helpful to investigate the spectroscopic variability of quasars and find unusual quasars.

2.2. *Pipeline for Data Reduction*

The raw CCD images after observations were reduced by the LAMOST two-dimensional (2D) pipeline and one-dimensional (1D) pipeline, which is described in Luo et al. (2015). In the 2D pipeline, the raw data are processed and extracted to 1D spectra by the reduced procedure, including dark and bias subtraction, flat-field correction, cosmic-ray removal, spectral tracing and extraction, sky subtraction, wavelength calibration, merging sub-exposure and combining blue and red spectra (Luo et al. 2012). Then through the 1D pipeline, these 1D spectra are automatically classified into four primary categories: "STAR", "GALAXY", "QSO", and "Unknown" by template matching. The final spectra are available at the LAMOST Data Archive Server [1] (DAS).

The 1D pipeline classification is not trustworthy for the "Unknown" type. The main reason is that these "Unknown" spectra are taken under non-photometric conditions, e.g., varying seeing and/or cloudy weather. In addition, unstable efficiencies of some fibers also contribute to the high fraction of "Unknown" objects. In the LAMOST early data release, only $\sim 14\%$ of the observed quasar candidates are classified as QSO, STAR, or GALAXY by pipeline, while the majority of the spectra are categorized as "Unknown" (Paper I). Such high fraction of unrecognizable objects is due to the poor spectral quality in the early data release. Fortunately, the observation conditions in later years have been improved since the first year of regular survey, and the pipeline has been updated for a better performance of spectral classification. The fraction of candidates classified as "QSO" keeps relatively high in later regular survey (55.9% in Paper II, 62.3% in Paper III and 77.0% in this work).

2.3. *Quasar Identification*

In this work, the quasars are identified by visual inspections. In addition to the observed spectra of quasar candidates, the spectra that are classified as "QSO" by the 1D pipeline but not included in the input quasar candidate catalog also need visual inspection. With the help of a Java program ASERA (Yuan et al. 2013), we visually inspect these spectra based on typical quasar emission lines. Each spectrum is inspected by at least two classifier to check if the spectral features can match the quasar template. The misclassified spectra are rejected or reclassified. The redshift of each identified quasar is determined when the available typical quasar emission lines (e.g., as Hα, Hβ, O IIIλ5007, Mg II, C III and C IV) and templates were best matched . The "ZWARNING = 1" flag indicates there is only one emission line available. The quasars overlap with M31/M33 and Galactic center will be published in the work of background quasar survey (Huo et al. 2010, 2013, 2015 and so on), and are not included in our final quasar catalog. Finally, there are in total 13,255 visually confirmed quasars at quasar catalog. Among these identified quasars, 6,385 are known ones in the SDSS DR14 quasar catalog or Million Quasars catalog, while the remaining 6,870 are newly discovered. Since the LAMOST DR6 quasar candidate survey were fished in the same year as the SDSS DR14 quasar catalog was published, the 418 quasars in LAMOST DR6 cross-math with SDSS DR14 are considered as independently discovered by LAMOST. So at last, there are in total 7288 quasars that were independently discovered by LAMOST. With a large number of repeat spectral observations of SDSS and LAMOST, we can investigate the spectroscopic variability of quasars on both short and long time scale. Moreover, these multi-epoch spectra give us a good chance to search for unusual AGNs such as changing-look AGNs (CL-AGNs, Runco et al. 2016; MacLeod et al. 2019; Yang et al. 2018; Wang et al. 2019; Guo et al. 2019) and uncover the physical mechanism behind them (MacLeod et al. 2019; Frederick et al. 2019; Jin et al. 2022). The result of quasar identification is summarized in Table 1.

Table 1. The result of LAMOST quasars survey in DR6, 7, 8 and 9.

	DR6	DR7	DR8	DR9	Total
Total	4307	2305	3907	2736	13255
Independent	2277	890	2246	1875	7288
New	1859	890	2246	1875	6870

Figure 1 shows the distribution of the redshift and absolute luminosity, which is represented by the K-corrected i-band absolute magnitudes M_i ($z = 2$), normalized at $z = 2$ (Richards et al. 2006). As can be seen, there is a drop in the redshift distribution at $z \sim 1$, which is similar to the previous results (Papers I, II and III). This drop is the result of inefficient identification in this redshift range when the emission line Mg II moves into the overlap region of the blue and red channels. For the sources observed by both SDSS and LAMOST, only

---

[1] http://www.lamost.org/lmusers/

88 of them have redshift difference (Δz) greater than 0.1. The difference mainly comes from the misidentification of emission lines in LAMOST spectra due to the low S/N. As shown in Figure 2, it is clearly that as the S/N decreases, the Δz increases. Another reason for the redshift difference is that we estimated the redshift based on the strongest typical emission line, while the redshift values in SDSS are measured with a few difference approaches, such as principal component analysis (PCA) or Mg II emission line (Pâris et al. 2018).

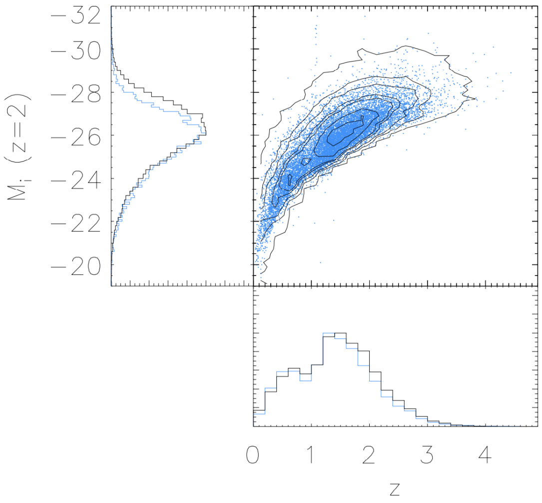

Figure 1. The distribution in the magnitude-redshift space for the visually confirmed quasars for previous LAMOST quasar survey (black) and in DR 6&7&8&9 (blue). The absolute magnitudes $M_i(z=2)$ are normalized at z=2, following the K-correction of Richards et al. (2006). The left and bottom panels show the distributions as normalized histograms.

3. SPECTRAL ANALYSIS

In this section, we describe the spectral analysis, which includes the absolute flux-calculation, the measurements of typical quasar emission lines, and the estimations of black hole masses.

3.1. *Absolute Flux Calculation*

We note that LAMOST is only equipped with a spectrograph and cannot provide photometric information for the observed targets (Xiang et al. 2015). Thus, the released LAMOST spectra only have relative flux calibration rather than absolute flux calibration. In this work, we try to achieve the absolute calibration by scaling each spectrum to the corresponding broad-band photometric measurements. The broad-band photometry used in this work is the PSF magnitudes from the SDSS or Pan-STARRS. First, we cross-match the LAMOST objects with the SDSS photometric database with a $3''$-matching radius. The sources outside the SDSS footprint are then cross-matched with Pan-STARRS with the same matching radius [2]. Due to the limitation of spectral wavelength coverage, we only use g,r,i-band during the calibration fitting. The magnitudes in these three bands are converted into the flux density f_λ at the effective wavelength of each filter. Next, we fit each quasar spectrum with the flux densities in three bands. The spectra from the blue and red channels are fitted separately to correct the sudden flux jump near the wavelength overlap region when the blue and red channel spectra are improperly stacked. The fits are based on the IDL routines in the `MPFIT` package (Markwardt 2009), which performs the χ^2 minimization using the Levenberg-Marquardt method. Examples of the fitting results are presented in Figure 3. It is clearly that the sudden change between the blue and red regions in the original spectrum disappears after the flux re-calibration.

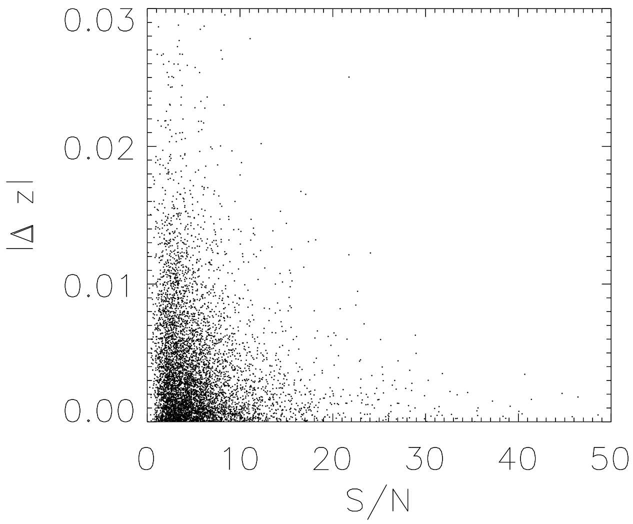

Figure 2. The distribution of Δz for common quasars between this work and SDSS versus LAMOST spectral S/N.

The quasars usually show optical variabilities with 0.1-0.2 mag, which introduce additional uncertainties into the absolute flux-calibration. However, the spectra without the absolute flux calibration information can not be used to obtain important quantities in-

---

[2] The 8 identified QSOs spectra that don't have reliable SDSS or Panstarrs photometric informations are not flux calibrated in this work.

cluding continuum luminosity, black hole mass (M_{BH}), emission line flux. In the previous paper of LAMOST quasar survey (Papers I, II and II), the spectra are not absolute-flux-calibrated, the continuum luminosity is inferred from the model fitting with the SDSS photometric data, and there are no emission line flux informations in the published catalogs. Additionally, a small fraction of spectra ($\sim$ 17% in Paper II and $\sim$ 6% in Paper III) cannot be fitted properly due to the sudden flux jump near the overlap region, which is solved by the absolute flux-calibration in this work. Despite the uncertainties of our absolute flux-calibration, it nevertheless helps understand more about the central BHs.

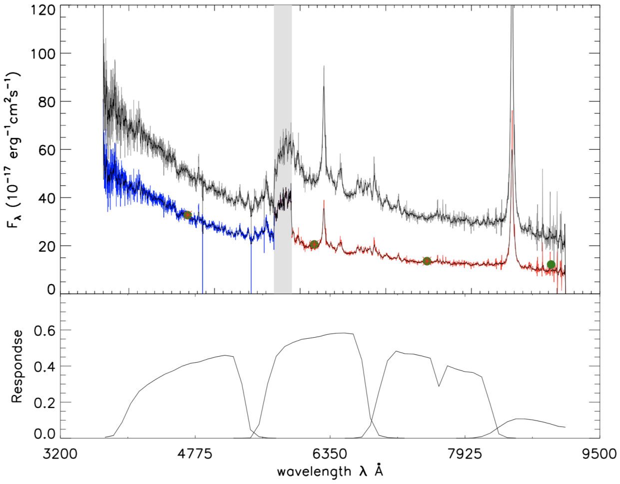

Figure 3. An example of SDSS photometry fitting for the blue- and red-arm LAMOST spectra. Top panel: the gray spectrum is the original spectrum only with the relative flux calibration. The green dots represent the flux densities in the g, r, i, z-bands, and the asterisks mark the flux densities are used during the fitting. The lines in blue and red represent piecewise fits to the asterisks. The vertical gray area represents the overlap region which is masked during the fitting. The bottom panel shows the filter curves for the SDSS in g, r, i, z-band. It is clear that the z-band is not fully covered by the spectrum, so the photometric data in z-band is not used during the spectral fitting.

3.2. *Spectral fitting*

Here we describe the fitting procedures for LAMOST quasar spectra. Before the fitting, each absolute flux calibrated spectrum is corrected for the Galactic extinction using the reddening map (Schlegel et al. 1998) and Milky Way extinction law of Fitzpatrick (1999) with $R_V = 3.1$, and then transformed into the rest-frame using the visually inspected redshift.

Then the spectra are fitted by the publicly avaiable multicomponent spectral fitting code `PYQSODFIT` (Guo et al. 2018) and a wrapper package based on it (`QSOFITMORE` , Fu et al. 2021). A detailed description of the code and its application can be found in Guo et al. (2018), Shen et al. (2019) and Fu et al. (2021).

3.2.1. *Continuum*

The pseudo continuum is fitted by a broken power law ($f_{\rm bpl}$) and Fe II model ($f_{\rm Fe,ii}$) in the wavelength windows without quasar emission lines and outside the LAMOST spectral overlapping region. During the fitting, the turning point of the broken power law is fixed at 4661 Å at rest-frame, which is similar to the value derived from the mean composite quasar spectra in Vanden Berk et al. (2001). The iron model $f_{\rm Fe,ii}$ is

$$f_{\rm Fe,ii} = \rm b_0 F_{Fe,ii}(\lambda, b_1, b_2), \qquad (1)$$

where the parameters b_0, b_1, b_2 are the normalization, the full width at half-maximum (FWHM) of Gaussian profile used to convolve the Fe,II template, and the wavelength shift applied to the Fe,II template, respectively. The optical Fe,II template is based on Boroson & Green (1992). The UV Fe,II template is a modified template consisting of the templates in the wavelength range of 1000-2000 Å based on Vestergaard & Wilkes (2001), 2200-3090 Å based on Salviander et al. (2007), and 3090-3500 Å based on Tsuzuki et al. (2006). A few spectra have peculiar shapes in the continuum, which may result from unstable efficiencies of some fibers and poor relative flux calibration because it is difficult to find a suitable flux standard star for each spectrograph, especially for our extragalactic targets because they are faint and located at high Galactic latitudes. In this case, we add a three-order poly-nomial model ($f_{\rm poly}$) component to solve this problem. At last, the $\rm f_{cont}$ is fitted by two (or three) components:

$$f_{\rm cont} = \rm f_{bpl} + f_{Fe,ii} + (f_{poly}). \qquad (2)$$

The host galaxy contamination is negligible for high z ($z \gtrsim 0.5$) or high luminosity ($\log L_{5100} \gtrsim 44.5$) quasars. As for the $z \lesssim 0.5$ low-luminosity quasars, the hosts on average can contribute $\sim$ 15% to the emissions and lead to a $\sim$ 0.06 dex overestimation of the 5100 Å continuum luminosity (Shen et al. 2011). However, due to the limitation of the spectral S/N for faint objects in our catalog, the process of host-subtraction may bring larger uncertainties. Therefore, in this work, the decomposion of the host galaxy is not applied to the spectrum.

The fitted pseudo-continuum component is subtracted from the spectrum and the remaining emission-line components are fitted with Gaussian profiles. Below we describe the detailed fitting procedures for typical quasar emission lines: Hα, Hβ, Mg II and C IV. They are the strongest broad emission lines in the available wavelength range, and are commonly used as virial black hole mass estimators. During the fitting, the parameters we mainly focus are FWHM, equivalent width (EW) and flux. The fitting procedures for each line are described as follows.

3.2.2. *Hα line*

The pseudo-continuum-subtracted Hα-[N II]-[S II] emission lines are fitted in the restframe windows [6350,6800] Å for objects at $z \lesssim 0.37$. The broad component of Hα is modeled by two Gaussian profiles, and the narrow components of Hα, [N II]$\lambda\lambda$6548,6584 and [S II]$\lambda\lambda$6716,6731 are modeled by a single Gaussian profile. The upper limit of FWHM for the narrow components is set to be 900km s^{-1}, which a commonly used the FWHM criterion adopted to separate the Type 1 and Type 2 AGNs (Wang et al. 2009; Coffey et al. 2019; Wang et al. 2019). The line widths and velocity offsets of the narrow lines are tied to each other. Relative flux for [N II]$\lambda\lambda$6548,6584 doublet is fixed to 2.96. Examples of the best-fitting results of Hα line are given in the panel (a) of Figure 4.

3.2.3. *Hβ line*

The pseudo-continuum-subtracted Hβ-[O III] emission lines are fitted in the restframe window [4600,5100] Å for objects at $z \lesssim 0.8$. Similar to Hα, the broad component of Hβ is modeled by two Gaussian profiles, and the narrow component of Hβ is modeled by a single Gaussian profile. The upper limit of FWHM for the narrow components is set to be 900km s^{-1}. In addition to a single narrow component, the [O III]$\lambda\lambda$,4959,5007 double lines require blue wing component as has been suggested by previous studies (Boroson 2005; Chadid et al. 2004; Komossa & Xu 2007; Zamfir et al. 2010; Schmidt et al. 2018). Therefor each of the [O III]$\lambda\lambda$,4959,5007 double lines is modeled by two Gaussians, one for a line core and the other for the blue shifted wing, and neither of them are tied to the Hβ narrow component. The line widths and velocity offsets of the cores and wings are tied to each other. We constrain the relative flux ratio of [O III]$\lambda\lambda$,4959,5007 double lines to be the theoretical ratio of 1:3. Examples of the best-fitting results of Hβ line are given in the panel (b) of Figure 4.

3.2.4. *Mg II line*

Fittings of the Mg II and C IV emission lines are sometimes affected by the broad and narrow absorption features. In order to reduce the effect of narrow absorption features, we used "rej_abs = True" option of the `QSOFITMORE` code when fitting Mg II and C IV emission lines. The code masks out the 3σ outliers below the continuum model, which is useful to reduce the impact of absorption features (Shen et al. 2011; Shin et al. 2019).

We fit the Mg II emission line for objects at $0.36 \lesssim z \lesssim 2.1$ in the spectral restframe range of [2700,2900] Å. The broad component of Mg II is modeled by two Gaussian profiles. As for the narrow component, the situation is more complicated. Some AGNs show the Mg II$\lambda\lambda$2796,2803 double lines around the peak, and the FWHM of each component is $\lesssim 750$ km s^{-1} (Shen et al. 2011). However, such cases are rare and most LAMOST spectra do not have adequate S/N and/or spectral resolution to separate these two components. Additionally, the narrow Mg II absorption line can lead to mimicking double peaks. So in this work, we fit the Mg II narrow component by a single narrow Gaussian with FWHM upper limit of 900km s^{-1}. Examples of the best-fitting results of Mg II line are given in the panel (c) of Figure 4.

3.2.5. *C IV line*

We fit the C IV emission line for objects at $1.5 \lesssim z \lesssim 4.4$ in the spectral restframe range of [1500,1700]Å. Similar to other emission lines, the broad component of C IV line is modeled by two Gaussian profiles. We do not set the upper limit for the FWHM of the narrow component because it is still debatable whether a strong narrow C IV component exists for most quasars (Assef et al. 2011; Denney 2012; Shen et al. 2019). In addition to the broad and narrow components, the parameters of the entire C IV profile are also given because: (1) it is not sure whether the narrow component subtraction is feasible for C IV emission line, and (2) the existing C IV virial estimators are calculated with the FWHM from entire C IV profile. Examples of the best-fitting results of C IV are given in panel (d) of Figure 4.

3.2.6. *The Reliability of the Spectral Fitting and Error Estimation*

After the automatic fitting procedures, we visually inspect the fitting results for each object. The fittings are acceptable for most of the spectra with high S/N. The bad fittings are mainly caused by low S/N of the spectra and the lack of good pixels in the fitting region. A flag is given for each line based on the visual inspection : `LINE_FLAG = 0` indicates an acceptable fitting and reliable measurement; `LINE_FLAG = -1` indicates a spurious fitting; `LINE_FLAG = -9999` indicates there are not enough good pixels in the fitting region due to the limitation of spectral quality or wavelength region. The broad absorption features can also affect the fitting results. Those features at Mg II and/or C IV are marked with `BAL_FLAG = 1`.

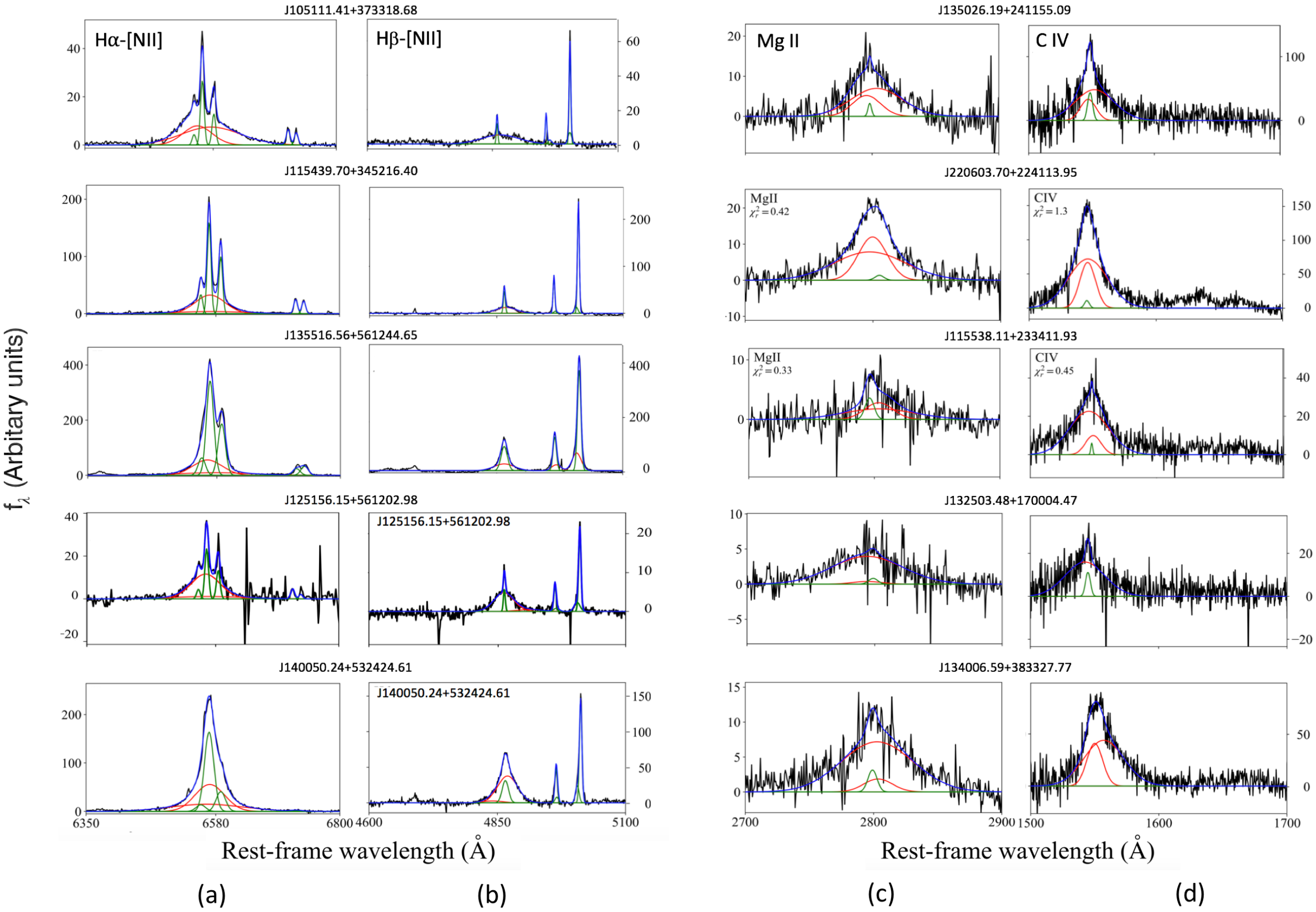

Figure 4. Examples for the deblending results of Hα-[N II]-[S II] (panel a), Hβ-[O III] (panel b), Mg II (panel c) and C IV (panel d) lines. The black lines represent the extinction-corrected spectra with continuum subtracted. As for the fitted emission lines, the broad components are in red while the narrow ones are in green, along with their sum (blue).

There are 4964/6296 quasars in our catalog overlapped with the spectral fitting catalog of DR7Q/DR14 (Shen et al. 2011, hereafter S11, and Rakshit et al. 2020, hereafter R20). To further justify the fitting results in this work, we compare the measured parameters for the common quasars between LAMOST DR 6&7&8&9 and (S11) R20. The histograms in Figure 5 compare the logarithm FWHM values. In general, we find excellent agreement between the measurements. The mean (μ) and standard deviation (σ) of the difference between this work and S11 (R20) is 0.10 ± 0.14 (0.06 ± 0.11) for Hα, 0.05 ± 0.14 (0.03 ± 0.14) for Hβ, 0.07 ± 0.13 (0.05 ± 0.12) for Mg II and 0.00 ± 0.12 (0.01 ± 0.12) for C IV lines. The EW values in these two catalogs are also in agreement with each other (Figure 6) with mean and standard deviation between two works is -0.10 ± 0.14 (-0.17 ± 0.13) for Hα, -0.10 ± 0.22 (-0.09 ± 0.20) for Hβ, 0.00 ± 0.17 (-0.09 ± 0.17) for Mg II and -0.05 ± 0.21 (-0.03 ± 0.20) for C IV lines. As mentioned before, there are no accurate emission flux information in the previous papers of the LAMOST quasars survey. In Figure 7, we show the comparison of the emission line flux measurements. The mean and standard deviation of the differences between this work and S11 (R20) is -0.15 ± 0.13 (-0.17 ± 0.15) for Hα, -0.09 ± 0.18 (-0.05 ± 0.18) for Hβ, 0.04 ± 0.17 (-0.04 ± 0.17) for Mg II and -0.03 ± 0.18 (-0.04 ± 0.20) for C IV lines. Similar to the FWHM and EW, the emission fluxes also show excellent agreement between the different measurements.

In all cases, though a slight discrepancy between the different works is found, the measurements in this work are in general agreement with those of SDSS. The differences may be caused by three main reasons: (1) quasars usually show spectral variability, which can affect the measurements in different quasar catalogs. (2) The different S/N of SDSS and LAMOST spectra. As shown in Figure 8, the peak of the median S/N per pixel in line-fitting regions are all around or below S/N =5. Figure

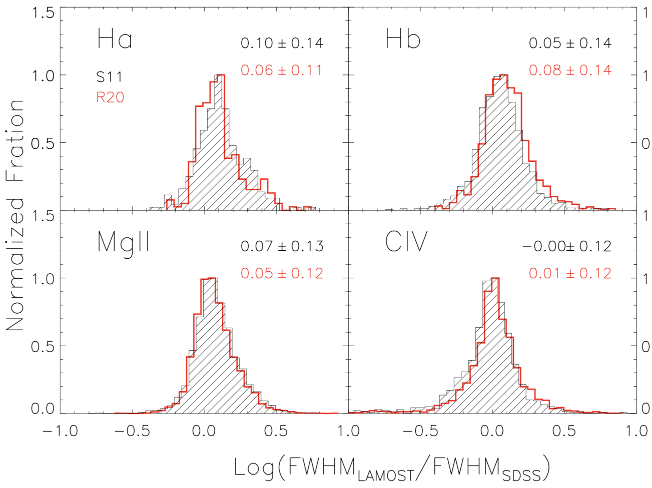

Figure 5. Comparisons between the measurements of the FWHM values in this work and S11 (R20). We show the plot of log(FWHM$_{\rm LAMOST}$/FWHM$_{\rm SDSS}$) for broad Hα (upper left), broad Hβ (upper right), broad Mg II (lower left) and total C IV (lower right). The mean (μ) and dispersion (σ) of each distribution are tabulated in corresponding plots. In this figure, only the emission lines with reliable fitting (`LINE_FLAG = 0`) are considered.

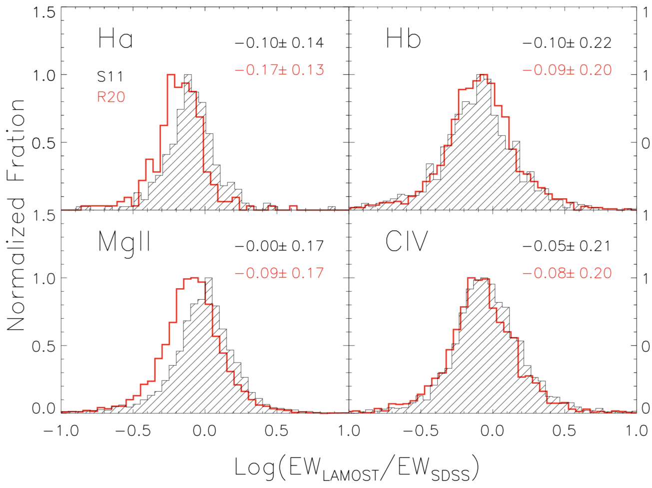

Figure 6. Same as in Figure 5, but for EW values.

9 shows the comparison of the median S/N per pixel of the line-fitting regions between LAMOST DR 6&7&8&9 and S11 (R20). It is clearly that the LAMOST spectra have significantly lower S/N than that those of SDSS. (3) the different model used in the spectral fitting. For example, in the continuum fitting process, the host-galaxy subtraction is applied in R20, and there is an additional Balmer continuum component in the pseudo-continuum.

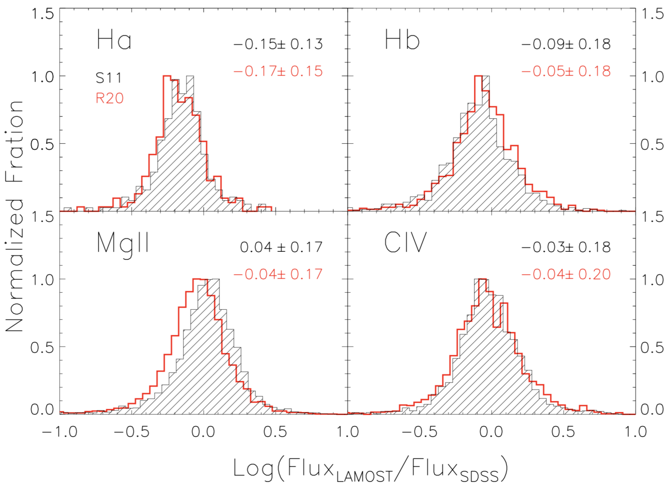

Figure 7. Same as in Figure 5, but for emission line flux.

The Fe II template (Vestergaard & Wilkes 2001) used in S11 is different from that in this work. There are also some differences in the emission-line fitting process: we used the double Gaussians to model the broad component in Hα, Hβ, Mg II and C IV emission lines, while in S11 or R20, multiple Gaussians (up to three) are used to fit each broad component. Moreover, in R20, there is no narrow component to model the C IV emission lines.

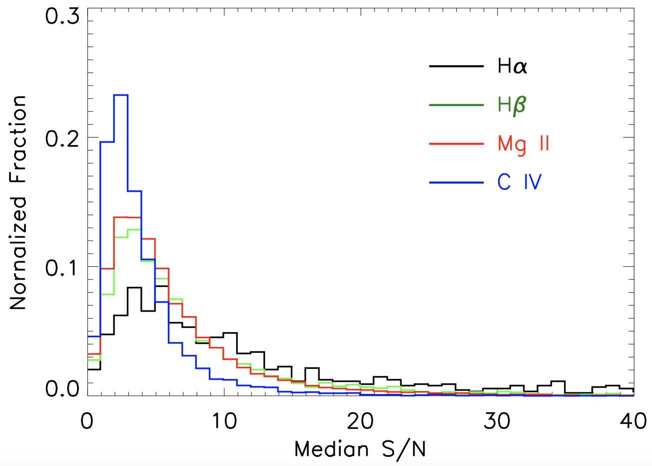

Figure 8. The distributions of median S/N per pixel around the line-fitting region are plotted as normalized histogram. Only the emission lines with reliable fitting (`LINE_FLAG = 0`) are considered.

The Monte Carlo (MC) approach is applied to estimate the uncertainty in each spectral fitting quantity. The mock spectrum is produced by adding a Gaussian random noise to the original spectrum. Then the spec-

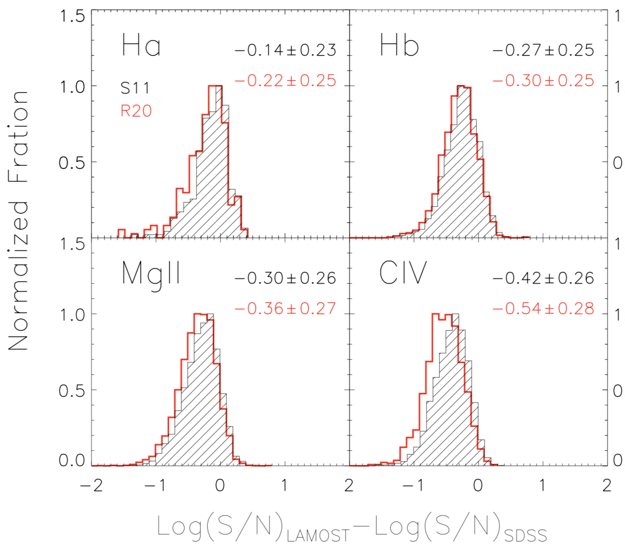

Figure 9. The comparison of the median S/N per pixel in the line-fitting region between this work and S11 (R20). The mean (μ) and dispersion (σ) of each distribution are shown in corresponding plots. Only the emission lines with reliable fitting (`LINE_FLAG = 0`) are considered.

tral fitting is performed to the mock spectrum and the spectral quantities are estimated. The uncertainty of each quantity is then estimated by the standard deviations of the distribution given by 50 trials.

3.3. *Virial Black hole Mass*

The monochromatic continuum luminosities at 1350 (L_{1350}), 3000 (L_{3000}), and 5100 (L_{5100}) Å are calculated from the best-fit $f_{\rm bpl}$ + (f$_{\rm poly}$) continuum. The bolometric correction factors are adapted from Richards et al. (2006). By assuming the broad line region (BLR) is virialized, the M$_{\rm BH}$ can be estimated based on the single-epoch spectra. The monochromatic continuum luminosity is used as a proxy of the BLR radius, and the broad line width is used as a proxy of the virial velocity. The empirical scaling relation between the virial black hole mass and these two proxies are calibrated by reverberation mapping. Here, the Hβ-based virial black hole masses are estimated using the relation (Vestergaard & Peterson 2006):

$$\log M_{\rm BH} = \log\left\{\left[\frac{\rm FWHM(H\beta)}{\rm km\,s^{-1}}\right]^2\left[\frac{L_{5100}}{10^{44}\,{\rm ergs\,s^{-1}}}\right]^{0.5}\right\} + 0.91, \tag{3}$$

the Mg II-based virial black hole masses are estimated using the relation (Wang et al. 2009):

$$\log M_{\rm BH} = \log\left\{\left[\frac{\rm FWHM(Mg\,II)}{\rm km\,s^{-1}}\right]^{1.51}\left[\frac{L_{3000}}{10^{44}\,{\rm ergs\,s^{-1}}}\right]^{0.5}\right\} + 2.60, \tag{4}$$

and the C IV-based virial black hole masses are estimated using the relation (Vestergaard & Peterson 2006):

$$\log M_{\rm BH} = \log\left\{\left[\frac{\rm FWHM(C\,IV)}{\rm km\,s^{-1}}\right]^{2}\left[\frac{L_{1350}}{10^{44}\,{\rm ergs\,s^{-1}}}\right]^{0.53}\right\} + 0.66. \tag{5}$$

As mentioned before, the spectra is re-calibrated using the photometric data observed at different times from LAMOST observations, which will introduce additional uncertainties. To justify this effect, we compare our continuum luminosities and M$_{\rm BH}$ measurements with those of S11 (R20) in Figure 10. In general, our estimates are in agreement with those of S11 (R20). Figure 11 shows the distribution of the M$_{\rm BH}$ at different redshifts. Most quasars observed in SDSS DR7Q have low-to-moderate redshifts, which is similar to the LAMOST survey. While in SDSS DR14Q, compared with SDSS DR7Q, there are larger number of hight-redshift and low-luminosity quasars observed. So it is apparent that the overall distribution of LAMOST quasars occupies the similar space as SDSS DR7Q, but has a relatively large discrepancy from SDSS DR14Q. The comparisons in both Figure 10 and Figure 11 prove that the flux re-calibration is mostly valid and the M$_{\rm BH}$ given in this work can be considered as a good approximation.

4. DESCRIPTION OF THE CATALOG

We provide a compiled catalog for the quasars identified in LAMOST DR 6&7&8&9 along with this paper. All measured quantities are tabulated in the online catalog at LAMOST public website[3]. A summary of parameters are listed in Table 2 and described as below.

1. Unique spectra ID in LAMOST database.
2. Target Observation date.
3. LAMOST object designation: Jhhmmss.ss + ddmmss.s (J2000).

4-5. Right Ascension and Declination (in decimal degrees, J2000).

---

[3] https://nadc.china-vo.org/data/article/20190107155838;jsessionid=F0A7D quasar&intro=%2Farticle%2F20190107155838

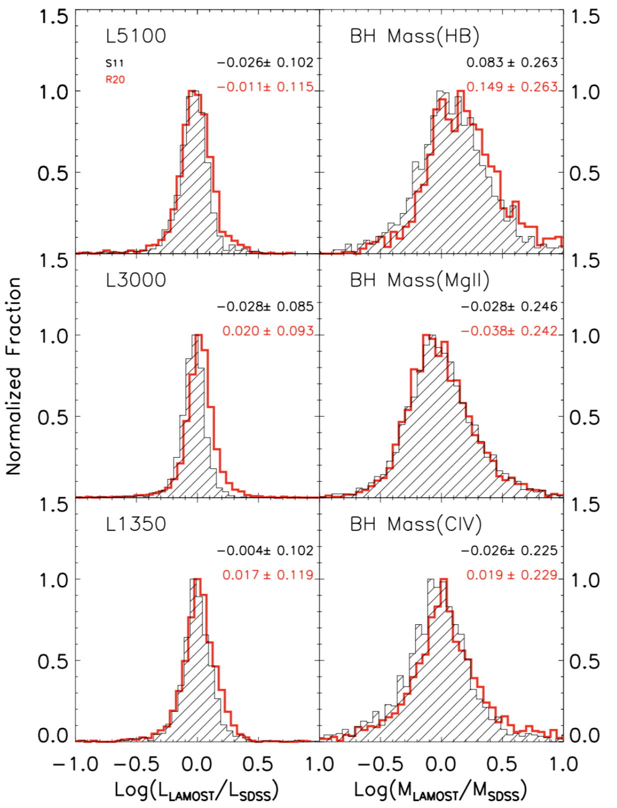

Figure 10. The comparison of the monochromatic continuum luminosities (L_{5100}, L_{1000}, L_{1300}) and the estimated $\mathrm{M_{BH}}$ based on Hβ, Mg II and C IV between this work and S11 (R20).

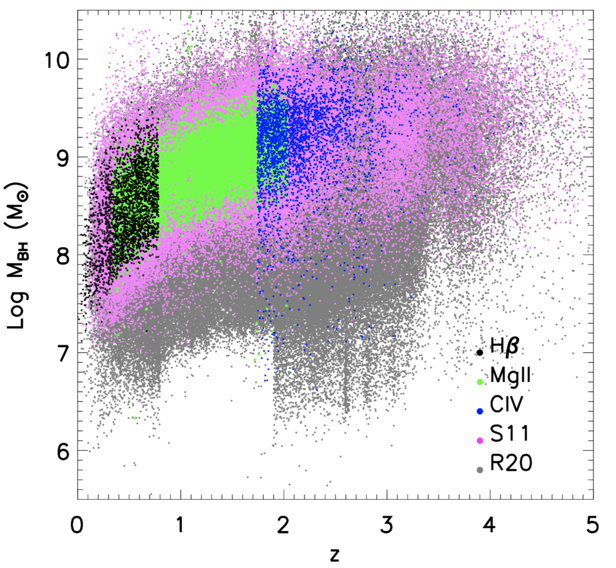

Figure 11. The distribution of $\mathrm{M_{BH}}$ based on various broad emissions (Hβ, Mg II and C IV) is plotted against the redshift. The quasars from S11 and R20 are represented by the pink and gray dots, respectively.

6-9. Spectroscopic observation information: Local modified Julian date (LMJD), spectroscopic plan name (PlanID), spectrograph identification (spID), and spectroscopic fiber number (fiberID). These four numbers are unique for each spectrum named in the format of spec−LMJD−planID_spID−fiberID.fits.

10-11. Redshift and its flag (ZWARNING) based on visual inspections. 1=not robust (eg., only one emission line available).

12. Target selection flag. SOURCE_FLAG="1" indicates that the quasar was selected by its infrared-optical color, data-mining algorithms, multi-wavelength or other serendipitous algorithms. SOURCE_FLAG="0" means the object is not included in LAMOST quasar survey candidate sample but identified as quasar.

13. $\mathrm{M_i}$ (z = 2): absolute i-band magnitude with K-corrected to $z = 2$ following Richards et al. (2006).

14. Number of spectroscopic observations for the quasar. When there are more than one observations for the object, the line properties are obtained from only one of the observations in which the S/N is highest.

15. Median S/N per pixel in the continuum wavelength regions.

16. Flag of broad absorption features. BAL_FLAG=1 indicates broad absorption features are present in Mg II and/or C IV.

17-46. FLUX, FWHM, rest-frame EW, and their uncertainties for broad Hα, narrow Hα, [N II]λ6584 and [S II]$\lambda\lambda$6716,6731 emission lines.

47-48. Number of good pixels and median S/N per pixel for the spectrum in Hα region of rest-frame 6350-6800 Å.

49. Flag indicates reliability of the emission line fitting results in Hα region upon visual inspections. 0=acceptable; -1=unacceptable. This value is set to be −9999 if Hα is not measured due to too few good pixels in the fitting region.

50-67. FLUX, FWHM, rest-frame EW, and their uncertainties for broad Hβ, narrow Hβ, [O III]$\lambda\lambda$5007 emission lines.

68-69. Number of good pixels and median S/N per pixel for the spectrum in Hβ region of rest-frame 4600-5100 Å.

70. Flag indicates reliability of the emission line fitting results in Hβ region upon visual inspections. 0=acceptable; -1=unacceptable. This value is set

to be −9999 if Hβ is not measured due to too few good pixels in the fitting region.

71-82. FLUX, FWHM, rest-frame EW, and their uncertainties for the broad and narrow Mg II emission line.

83-84. Number of good pixels and median S/N per pixel for the spectrum in Mg II region of rest-frame 2700-2900 Å.

85. Flag indicates reliability of the emission line fitting results in Mg II region upon visual inspections. 0=acceptable; -1=unacceptable. This value is set to be −9999 if Mg II is not measured due to too few good pixels in the fitting region.

86-103. FLUX, FWHM, rest-frame EW, and their uncertainties for the whole, broad and narrow C IV emission line.

104-105. Number of good pixels and median S/N per pixel for the spectrum in C IV region of rest-frame 1500-1700 Å.

106. Flag indicates reliability of the emission line fitting results in C IV region upon visual inspections. 0=acceptable; -1=unacceptable. This value is set to be −9999 if C IV is not measured due to too few good pixels in the fitting region.

107. Wavelength power-law index, α_λ, from blueward of 4661 Å.

108. Wavelength power-law index, α_λ, from redward of 4661 Å.

109. Rest-frame normalization parameter of optical Fe II.

110. Rest-frame Gaussian FWHM of optical Fe II complex.

111. Rest-frame wavelength shift of optical Fe II complex.

112. Rest-frame normalization parameter of UV Fe II complex.

113. Rest-frame Gaussian FWHM of UV Fe II complex.

114. Rest-frame wavelength shift of UV Fe II complex.

115-120. Monochromatic luminosities and their uncertanties at 1350, 3000 and 5100 Å.

121-123. Virial black hole masses (in $M_\odot$) with calibrations of Hβ, Mg II and C IV.

124 Name of the quasar in SDSS quasar catalog. The LAMOST DR 6&7&8&9 quasar catalog was cross-correlated with the SDSS quasar catalog (DR14, Pâris et al. 2018) using a matching radius of 3″.

125. Name of the object in second ROSAT all-sky survey point source catalog (2RXS, Boller et al. 2016). The LAMOST DR 6&7&8&9 quasar catalog was cross-correlated with 2RXS using a matching radius of 30″. The nearest point source in 2RXS was chosen.

126-127. The background corrected source counts in full band (0.1-2.4 keV), and its error, from 2RXS.

128. The exposure time of the ROSAT measurement.

129. Angular separation between the LAMOST and 2RXS source positions.

130. Name of the object in XMM-Newton Serendipitous Source Catalog . The LAMOST DR6&7&8&9 quasar catalog was cross-correlated with XMM-Newton Serendipitous Source Catalog (4XMM-DR11, Webb et al. 2020) using a matching radius of 3″.

131-132. The mean full-band (0.2-12 keV) flux, and its error, from 4XMM-DR11.

133. Angular separation between the LAMOST and 4XMM-DR11 source positions.

134. FIRST peak flux density at 20 cm in units of mJy. The LAMOST DR 6&7&8&9 quasar catalog was cross-correlated with FIRST survey catalog using a matching radius of 5″.

135. Angular separation between LAMOST and FIRST source positions.

136-141. SDSS (or Pan-STARRS) g, r, i PSF magnitudes, and their uncertainties.

142. Flag of PSF magnitudes. ‘`MAG_FLAG=1`’ indicates the PSF magnitudes are given by SDSS, ‘`MAG_FLAG=0`’ indicates the PSF magnitudes are give by Pan-STARRS and ‘`MAG_FLAG=-1`’ indicates that the quasars don‘t have reliable photometric information.

Table 2. Catalog format for the quasars identified in LAMOST DR6&7&8

Column	Name	Format	Description
1	ObsID	LONG	Unique Spectra ID in LAMOST database
2	ObsDate	STRING	Target observation date
3	NAME	STRING	LAMOST designation hhmmss.ss+ddmmss (J2000)

Table 2 continued

Table 2 *(continued)*

Column	Name	Format	Description
4	RA	DOUBLE	Right ascension (R.A.) in decimal degrees (J2000)
5	DEC	DOUBLE	Declination (Decl.) in decimal degrees (J2000)
6	LMJD	LONG	Local Modified Julian Day of observation
7	PLANID	STRING	Spectroscopic plan identification
8	SPID	LONG	Spectrograph identification
9	FIBERID	LONG	Spectroscopic fiber number
10	Z_VI	DOUBLE	Redshift based on visual inspection
11	ZWARNING	LONG	ZWARNING flag based on visual inspection
12	SOURCE_FLAG	LONG	Flag of quasar candidate selection
13	MI_Z2	DOUBLE	$M_i(z=2)$, K-corrected to $z=2$ following Richards et al. (2006)
14	NSPECOBS	LONG	Number of spectroscopic observations
15	SNR_SPEC	DOUBLE	Median S/N per pixel of the spectrum
16	BAL_FLAG	LONG	Flag of broad absorption features
17	FLUX_BROAD_HA	DOUBLE	Flux of broad Hα in erg s^{-1}
18	ERR_FLUX_BROAD_HA	DOUBLE	Uncertainty in $\mathrm{FLUX}_{\mathrm{H}\alpha,\mathrm{broad}}$
19	FWHM_BROAD_HA	DOUBLE	FWHM of broad Hα in km s^{-1}
20	ERR_FWHM_BROAD_HA	DOUBLE	Uncertainty in $\mathrm{FWHM}_{\mathrm{H}\alpha,\mathrm{broad}}$
21	EW_BROAD_HA	DOUBLE	Rest-frame EW of broad Hα in Å
22	ERR_EW_BROAD_HA	DOUBLE	Uncertainty in $\mathrm{EW}_{\mathrm{H}\alpha,\mathrm{broad}}$
23	FLUX_NARROW_HA	DOUBLE	Flux of narrow Hα in erg s^{-1}
24	ERR_FLUX_NARROW_HA	DOUBLE	Uncertainty in $\mathrm{FLUX}_{\mathrm{H}\alpha,\mathrm{narrow}}$
25	FWHM_NARROW_HA	DOUBLE	FWHM of narrow Hα in km s^{-1}
26	ERR_FWHM_NARROW_HA	DOUBLE	Uncertainty in $\mathrm{FWHM}_{\mathrm{H}\alpha,\mathrm{narrow}}$
27	EW_NARROW_HA	DOUBLE	Rest-frame EW of narrow Hα in Å
28	ERR_EW_NARROW_HA	DOUBLE	Uncertainty in $\mathrm{EW}_{\mathrm{H}\alpha,\mathrm{narrow}}$
29	FLUX_NII_6584	DOUBLE	Flux of [N II]λ6584 in erg s^{-1}
30	ERR_FLUX_NII_6584	DOUBLE	Uncertainty in $\mathrm{FLUX}_{\mathrm{[NII]6584}}$
31	FWHM_NII_6584	DOUBLE	FWHM of [N II]λ6584 in km s^{-1}
32	ERR_FWHM_NII_6584	DOUBLE	Uncertainty in $\mathrm{FWHM}_{\mathrm{[NII]6584}}$
33	EW_NII_6584	DOUBLE	Rest-frame EW of [N II]λ6584 in Å
34	ERR_EW_NII_6584	DOUBLE	Uncertainty in $\mathrm{EW}\ _{\mathrm{[NII]6584}}$
35	FLUX_SII_6716	DOUBLE	Flux of [S II]λ6716 in erg s^{-1}
36	ERR_FLUX_SII_6716	DOUBLE	Uncertainty in $\mathrm{FLUX}_{\mathrm{[SII]6716}}$
37	FWHM_SII_6716	DOUBLE	FWHM of [S II]λ6716 in km s^{-1}
38	ERR_FWHM_SII_6716	DOUBLE	Uncertainty in $\mathrm{FWHM}_{\mathrm{[SII]6716}}$
39	EW_SII_6716	DOUBLE	Rest-frame EW of [S II]λ6716 in Å
40	ERR_EW_SII_6716	DOUBLE	Uncertainty in $\mathrm{EW}\ _{\mathrm{[SII]6716}}$
41	FLUX_SII_6731	DOUBLE	Flux of [S II]λ6731 in erg s^{-1}
42	ERR_FLUX_SII_6731	DOUBLE	Uncertainty in $\mathrm{FLUX}_{\mathrm{[SII]6731}}$
43	FWHM_SII_6731	DOUBLE	FWHM of [S II]λ6731 in km s^{-1}
44	ERR_FWHM_SII_6731	DOUBLE	Uncertainty in $\mathrm{FWHM}_{\mathrm{[SII]6731}}$
45	EW_SII_6731	DOUBLE	Rest-frame EW of [S II]λ6731 in Å
46	ERR_EW_SII_6731	DOUBLE	Uncertainty in $\mathrm{EW}_{\mathrm{[SII]6731}}$
47	LINE_NPIX_HA	LONG	Number of good pixels for the rest-frame 6350-6800 Å
48	LINE_MED_SN_HA	DOUBLE	Median S/N per pixel for the rest-frame 6350-6800 Å
49	LINE_FLAG_HA	LONG	Flag for the quality in Hα fitting
50	FLUX_BROAD_HB	DOUBLE	Flux of broad Hβ in erg s^{-1}
51	ERR_FLUX_BROAD_HB	DOUBLE	Uncertainty in $\mathrm{FLUX}_{\mathrm{H}\beta,\mathrm{broad}}$
52	FWHM_BROAD_HB	DOUBLE	FWHM of broad Hβ in km s^{-1}
53	ERR_FWHM_BROAD_HB	DOUBLE	Uncertainty in $\mathrm{FWHM}_{\mathrm{H}\beta,\mathrm{broad}}$
54	EW_BROAD_HB	DOUBLE	Rest-frame EW of broad Hβ in Å
55	ERR_EW_BROAD_HB	DOUBLE	Uncertainty in $\mathrm{EW}_{\mathrm{H}\beta,\mathrm{broad}}$
56	FLUX_NARROW_HB	DOUBLE	Flux of narrow Hβ in erg s^{-1}
57	ERR_FLUX_NARROW_HB	DOUBLE	Uncertainty in $\mathrm{FLUX}_{\mathrm{H}\beta,\mathrm{narrow}}$

Table 2 continued

Table 2 *(continued)*

Column	Name	Format	Description
58	FWHM_NARROW_HB	DOUBLE	FWHM of narrow Hβ in km s^{-1}
59	ERR_FWHM_NARROW_HB	DOUBLE	Uncertainty in FWHM$_{\mathrm{H\beta,narrow}}$
60	EW_NARROW_HB	DOUBLE	Rest-frame EW of narrow Hβ in Å
61	ERR_EW_NARROW_HB	DOUBLE	Uncertainty in EW$_{\mathrm{H\beta,narrow}}$
62	FLUX_OIII_5007	DOUBLE	Flux of [O III]λ5007 in erg s^{-1}
63	ERR_FLUX_OIII_5007	DOUBLE	Uncertainty in FLUX$_{\mathrm{[OIII]5007}}$
64	FWHM_OIII_5007	DOUBLE	FWHM of [O III]λ5007 in km s^{-1}
65	ERR_FWHM_OIII_5007	DOUBLE	Uncertainty in FWHM$_{\mathrm{[OIII]5007}}$
66	EW_OIII_5007	DOUBLE	Rest-frame EW of [O III]λ5007 in Å
67	ERR_EW_OIII_5007	DOUBLE	Uncertainty in EW$_{\mathrm{[OIII]5007}}$
68	LINE_NPIX_HB	LONG	Number of good pixels for the rest-frame 4600-5100 Å
69	LINE_MED_SN_HB	DOUBLE	Median S/N per pixel for the rest-frame 4600-5100 Å
70	LINE_FLAG_HB	LONG	Flag for the quality in Hβ fitting
71	FLUX_BROAD_MGII	DOUBLE	Flux of the broad Mg II in erg s^{-1}
72	ERR_FLUX_BROAD_MGII	DOUBLE	Uncertainty in FLUX$_{\mathrm{MgII,broad}}$
73	FWHM_BROAD_MGII	DOUBLE	FWHM of the broad Mg II in km s^{-1}
74	ERR_FWHM_BROAD_MGII	DOUBLE	Uncertainty in FWHM$_{\mathrm{MgII,broad}}$
75	EW_BROAD_MGII	DOUBLE	Rest-frame EW of the broad Mg II in Å
76	ERR_EW_BROAD_MGII	DOUBLE	Uncertainty in EW$_{\mathrm{MgII,broad}}$
77	FLUX_NARROW_MGII	DOUBLE	Flux of the narrow Mg II in erg s^{-1}
78	ERR_FLUX_NARROW_MGII	DOUBLE	Uncertainty in FLUX$_{\mathrm{MgII,narrow}}$
79	FWHM_NARROW_MGII	DOUBLE	FWHM of the narrow Mg IIλ in km s^{-1}
80	ERR_FWHM_NARROW_MGII	DOUBLE	Uncertainty in FWHM$_{\mathrm{MgII,narrow}}$
81	EW_NARROW_MGII	DOUBLE	Rest-frame EW of the narrow Mg II in Å
82	ERR_EW_NARROW_MGII	DOUBLE	Uncertainty in EW$_{\mathrm{MgII,narrow}}$
83	LINE_NPIX_MGII	LONG	Number of good pixels for the rest-frame 2700-2900 Å
84	LINE_MED_SN_MGII	DOUBLE	Median S/N per pixel for the rest-frame 2700-2900 Å
85	LINE_FLAG_MGII	LONG	Flag for the quality in MgII fitting
86	FLUX_CIV	DOUBLE	Flux of the whole C IV in erg s^{-1}
87	ERR_FLUX_CIV	DOUBLE	Uncertainty in Flux$_{\mathrm{CIV,whole}}$
88	FWHM_CIV	DOUBLE	FWHM of the whole C IV in km s^{-1}
89	ERR_FWHM_CIV	DOUBLE	Uncertainty in FWHM$_{\mathrm{CIV,whole}}$
90	EW_CIV	DOUBLE	Rest-frame EW of the whole C IV in Å
91	ERR_EW_CIV	DOUBLE	Uncertainty in EW$_{\mathrm{CIV,whole}}$
92	FLUX_BROAD_CIV	DOUBLE	Flux of the broad C IV in erg s^{-1}
93	ERR_FLUX_BROAD_CIV	DOUBLE	Uncertainty in Flux$_{\mathrm{CIV,broad}}$
94	FWHM_BROAD_CIV	DOUBLE	FWHM of the broad C IV in km s^{-1}
95	ERR_FWHM_BROAD_CIV	DOUBLE	Uncertainty in FWHM$_{\mathrm{CIV,broad}}$
96	EW_BROAD_CIV	DOUBLE	Rest-frame EW of the broad C IV in Å
97	ERR_EW_BROAD_CIV	DOUBLE	Uncertainty in EW$_{\mathrm{CIV,broad}}$
98	FLUX_NARROW_CIV	DOUBLE	Flux of the narrow C IV in erg s^{-1}
99	ERR_FLUX_NARROW_CIV	DOUBLE	Uncertainty in Flux$_{\mathrm{CIV,narrow}}$
100	FWHM_NARROW_CIV	DOUBLE	FWHM of the narrow C IV in km s^{-1}
101	ERR_FWHM_NARROW_CIV	DOUBLE	Uncertainty in FWHM$_{\mathrm{CIV,narrow}}$
102	EW_NARROW_CIV	DOUBLE	Rest-frame EW of the narrow C IV in Å
103	ERR_EW_NARROW_CIV	DOUBLE	Uncertainty in EW$_{\mathrm{CIV,narrow}}$
104	LINE_NPIX_CIV	LONG	Number of good pixels for the rest-frame 1500-1700 Å
105	LINE_MED_SN_CIV	DOUBLE	Median S/N per pixel for the rest-frame 1500-1700 Å
106	LINE_FLAG_CIV	LONG	Flag for the quality in CIV fitting
107	ALPHA_LAMBDA_1	DOUBLE	Wavelength power-law index from blueward of 4661 Å
108	ALPHA_LAMBDA_2	DOUBLE	Wavelength power-law index from redward of 4661 Å
109	Fe_op_norm	DOUBLE	The normalization applied to the optical Fe$_{\mathrm{II}}$ template
110	Fe_op_shift	DOUBLE	The Gaussian FWHM applied to the optical the Fe$_{\mathrm{II}}$ template
111	Fe_op_FWHM	DOUBLE	The wavelength shift applied to the optical Fe$_{\mathrm{II}}$ template

Table 2 continued

Table 2 *(continued)*

Column	Name	Format	Description
112	Fe_uv_norm	DOUBLE	The normalization applied to the ultraviolet $\mathrm{Fe_{II}}$ template
113	Fe_uv_shift	DOUBLE	The Gaussian FWHM applied to the ultraviolet the $\mathrm{Fe_{II}}$ template
114	Fe_uv_FWHM	DOUBLE	The wavelength shift applied to the ultraviolet $\mathrm{Fe_{II}}$ template
115	LOGL1350	DOUBLE	Monochromatic luminosity at 1350 Å in $\mathrm{erg\,s^{-1}}$
116	ERR_LOGL1350	DOUBLE	Uncertainty in $\mathrm{logL_{1350}}$
117	LOGL3000	DOUBLE	Monochromatic luminosity at 3000 Å in $\mathrm{erg\,s^{-1}}$
118	ERR_LOGL3000	DOUBLE	Uncertainty in $\mathrm{logL_{3000}}$
119	LOGL5100	DOUBLE	Monochromatic luminosity at 5100 Å in $\mathrm{erg\,s^{-1}}$
120	ERR_LOGL5100	DOUBLE	Uncertainty in $\mathrm{logL_{5100}}$
121	LOGBH_HB	DOUBLE	Virial BH mass ($\mathrm{M_{\odot}}$) based on Hβ
122	LOGBH_MgII	DOUBLE	Virial BH mass ($\mathrm{M_{\odot}}$) based on Mg II
123	LOGBH_CIV	DOUBLE	Virial BH mass ($\mathrm{M_{\odot}}$) based on C IV
124	SDSS_NAME	STRING	Name of the quasar in the SDSS quasar catalog
125	2RXS_NAME	STRING	Name of the object in the 2nd ROSAT all-sky survey point source catalog
126	2RXS_CTS	DOUBLE	Background corrected source counts in 0.1-2.4 keV from 2RXS source catalog
127	2RXS_ECTS	DOUBLE	Error of the source counts from 2RXS source catalog
128	2RXS_EXPTIME	DOUBLE	Source exposure time from 2RXS source catalog
129	LM_2RXS_SEP	DOUBLE	LAMOST-2RXS separation in arcsec
130	4XMM_NAME	STRING	Name of the object in XMM-Newton Serendipitous Source Catalog
131	4XMM_FLUX	DOUBLE	Flux in 0.2-12.0 keV band from 4XMM-DR11 (in $\mathrm{erg\,s^{-1}\,cm^{-2}}$)
132	4XMM_FLUX_ERR	DOUBLE	Error of the flux in 0.2-12.0 keV band from 4XMM-DR11 (in $\mathrm{erg\,s^{-1}\,cm^{-2}}$)
133	LM_4XMM_SEP	DOUBLE	LAMOST-4XMM separation in arcsec
134	FPEAK	DOUBLE	FIRST peak flux density at 20 cm in mJy
135	LM_FIRST_SEP	DOUBLE	LAMOST-FIRST separation in arcsec
136	g_mag	DOUBLE	SDSS (or Pan-STARRS PSF) g magnitudes
137	ERR_g_mag	DOUBLE	g PSF magnitude errors
138	r_mag	DOUBLE	SDSS (or Pan-STARRS) r PSF magnitudes
139	ERR_r_mag	DOUBLE	r PSF magnitude errors
140	i_mag	DOUBLE	SDSS (or Pan-STARRS) i PSF magnitudes
141	ERR_i_mag	DOUBLE	i PSF magnitude errors
142	MAG_FLAG	LONG	Flag of PSF magnitude

(This table is available in its entirety in FITS format.)

5. SUMMARY

In this work, we present the result of the LAMOST Quasar Survey in the sixth, seventh, eighth and ninth data releases. There are in total 13,255 visually confirmed quasars. Among the identified quasars, 6,385 were reported by the SDSS DR14 quasar catalog after our survey began, while the remaining 6870 are considered as newly discovered.

We applied the emission line measurements of Hα, Hβ, Mg II and C IV for each confirmed quasar. As the LAMOST spectra lack information of absolute flux calibration, we re-calibrate the spectra by fitting the SDSS/Pan-STARRS photometric data. The measured quantities are complied into the quasar catalog which is available on-line.

After nine-year regular survey (Ai et al. 2016, Dong et al. 2018, Yao et al. 2019, and this work), there are in total 56,364 identified quasars in the LAMOST quasar survey. Among them, 32,052 are independently discovered by LAMOST, and 24,312 are newly discovered (Table 3).

Table 3. The summary of the results of the LAMOST quasars survey up to now.

	Paper I	Paper II	Paper III	This Work	Total
Total	3921	19935	19253	13255	56364
Independent	1180	12126	11458	7288	32052
New	1180	8100	8162	6870	24312

The basic properties of quasars identified in LAMOST DR1 to DR9 are compared with SDSS quasars. Figure 12 presents the redshift distribution of quasars for each sample. Generally, the redshift of LAMOST sample is lower than that of S11 and R20, but it is overall much more similar to S11 with only 0.13 smaller in mean value . The distributions of $\mathrm{M_{BH}}$ and continuum luminosities ($\mathrm{L_{5100}}$, $\mathrm{L_{3000}}$ and $\mathrm{L_{1350}}$) of LAMOST quasars are also compared with those of S11 and R20 in Figure 13. As for the continuum luminosities of LAMOST sample, the

L_{5100} is higher than S11 and R20, the L_{3000} is similar to S11, while the L_{1350} is similar to R20. The distribution of Hβ-based M_{BH} in LAMOST sample is similar to R20, while the Mg II- and C IV-based M_{BH} in LAMOST sample are similar to S11. These distributions indicate that the LAMOST quasars in lower redshift are more brighter with lower M_{BH}.

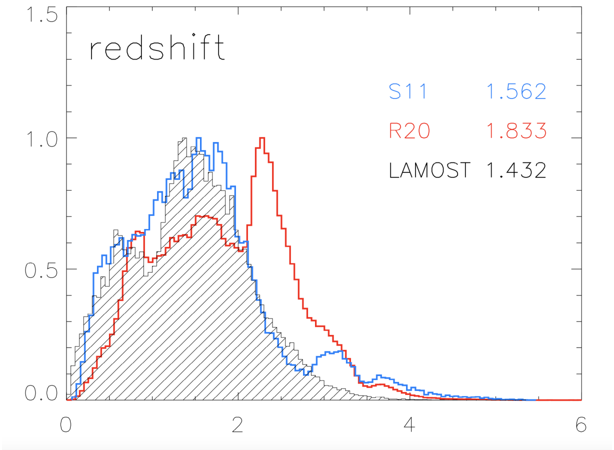

Figure 12. The redshift distributions of LAMOST (black) and SDSS (blue for S11, and red for R20) samples. The mean redshifts are tabulated in the top-right corner.

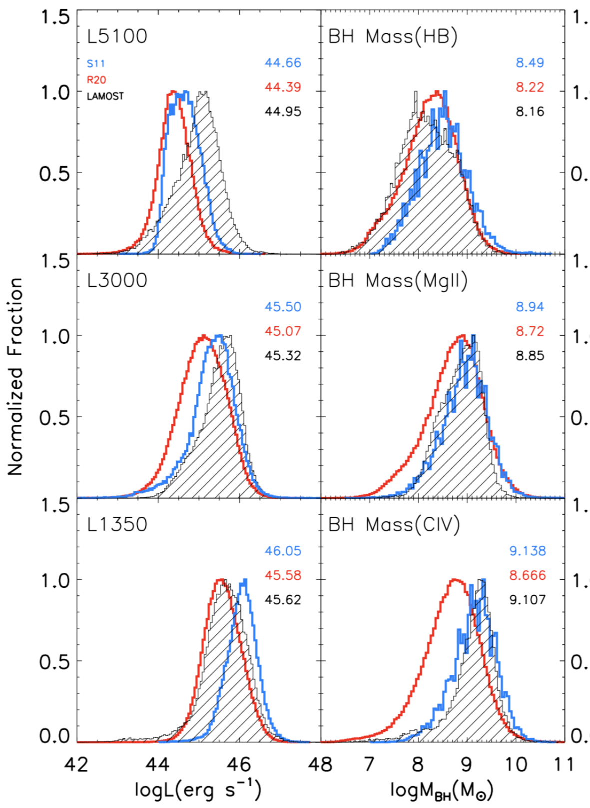

Figure 13. The histograms of the monochromatic continuum luminosities (L_{5100}, L_{1000}, L_{1300}) and the estimated M_{BH} (based on Hβ, Mg II and C IV) for LAMOST and S11 (R20) quasar sample. The mean value of each distribution is tabukated in the top-right corner.

The quasar catalog provided by LAMOST is not only a great supplement to the low-to-moderate redshift quasars, but also a large database for investigating the quasar spectral variabilities and searching for unusual quasars, such as the CL-AGNs (Yang et al. 2018).

This work is supported by the Ministry of Science and Technology of China under grant 2016YFA0400703, the NSFC grants No.11721303 and 11533001. The author acknowledges the support by the China Postdoctoral Science Foundation (2021M690229).

Guoshoujing Telescope (the Large Sky Area Multi-Object Fiber Spectroscopic Telescope LAMOST) is a National Major Scientific Project built by the Chinese Academy of Sciences. Funding for the project has been provided by the National Development and Reform Commission. LAMOST is operated and managed by the National Astronomical Observatories, Chinese Academy of Sciences.

This publication makes use of data products from the Sloan Digital Sky Survey. Funding for the Sloan Digital Sky Survey IV has been provided by the Alfred P. Sloan Foundation, the U.S. Department of Energy Office of Science, and the Participating Institutions. SDSS-IV acknowledges support and resources from the Center for High-Performance Computing at the University of Utah. The SDSS web site is www.sdss.org.

This work has made use of SDSS spectroscopic data. Funding for SDSS-III has been provided by the Alfred P. Sloan Foundation, the Participating Institutions, the National Science Foundation, and the U.S. Department of Energy Office of Science. The SDSS-III website is http://www.sdss3.org/. SDSS-III is managed by the Astrophysical Research Consortium for the Participating Institutions of the SDSS-III Collaboration, including the University of Arizona, the Brazilian Participation Group, Brookhaven National Laboratory, Carnegie Mellon University, University of Florida, the French Participation Group, the German Participation Group, Harvard University, the Instituto de Astrofisica de Canarias, the Michigan State/Notre Dame/ JINA Participation Group, Johns Hopkins University, Lawr- ence Berkeley National Laboratory, Max Planck Institute for Astrophysics, Max Planck Institute for Extraterrestrial

Physics, New Mexico State University, New York University, Ohio State University, Pennsylvania State University, University of Portsmouth, Princeton University, the Spanish Participation Group, University of Tokyo, University of Utah, Vanderbilt University, University of Virginia, University of Washington, and Yale University.

REFERENCES

Ai, Y. L., Wu, X.-B., Yang, J., et al. 2016, AJ, 151, 24. doi:10.3847/0004-6256/151/2/24

Ahn, C. P., Alexandroff, R., Allende Prieto, C., et al. 2012, ApJS, 203, 21. doi:10.1088/0067-0049/203/2/21

Andrei, A. H., Souchay, J., Zacharias, N., et al. 2009, A&A, 505, 385. doi:10.1051/0004-6361/200912041

Antonucci, R. 1993, ARA&A, 31, 473. doi:10.1146/annurev.aa.31.090193.002353

Assef, R. J., Denney, K. D., Kochanek, C. S., et al. 2011, ApJ, 742, 93. doi:10.1088/0004-637X/742/2/93

Bailer-Jones, C. A. L., Fouesneau, M., & Andrae, R. 2019, MNRAS, 490, 5615. doi:10.1093/mnras/stz2947

Becker, R. H., Fan, X., White, R. L., et al. 2001, AJ, 122, 2850. doi:10.1086/324231

Boller, T., Freyberg, M. J., Trümper, J., et al. 2016, A&A, 588, A103. doi:10.1051/0004-6361/201525648

Boyle, B. J., Shanks, T., Croom, S. M., et al. 2000, MNRAS, 317, 1014. doi:10.1046/j.1365-8711.2000.03730.x

Bovy, J., Hennawi, J. F., Hogg, D. W., et al. 2011, ApJ, 729, 141. doi:10.1088/0004-637X/729/2/141

Boroson, T. A. & Green, R. F. 1992, ApJS, 80, 109. doi:10.1086/191661

Boroson, T. 2005, AJ, 130, 381. doi:10.1086/431722

Carballo, R., Cofiño, A. S., & González-Serrano, J. I. 2004, MNRAS, 353, 211. doi:10.1111/j.1365-2966.2004.08056.x

Clowes, R. G. 1986, Mitteilungen der Astronomischen Gesellschaft Hamburg, 67, 174

Chadid, M., Wade, G. A., Shorlin, S. L. S., et al. 2004, A&A, 413, 1087. doi:10.1051/0004-6361:20031600

Coffey, D., Salvato, M., Merloni, A., et al. 2019, A&A, 625, A123. doi:10.1051/0004-6361/201833996

Cui, X.-Q., Zhao, Y.-H., Chu, Y.-Q., et al. 2012, Research in Astronomy and Astrophysics, 12, 1197. doi:10.1088/1674-4527/12/9/003

Denney, K. D. 2012, ApJ, 759, 44. doi:10.1088/0004-637X/759/1/44

Dong, X. Y., Wu, X.-B., Ai, Y. L., et al. 2018, AJ, 155, 189. doi:10.3847/1538-3881/aab5ae

Fan, X. 1999, AJ, 117, 2528. doi:10.1086/300848

Fan, X., White, R. L., Davis, M., et al. 2000, AJ, 120, 1167. doi:10.1086/301534

Feissel, M. & Mignard, F. 1998, A&A, 331, L33

Ferrarese, L., & Merritt, D. 2000, ApJL, 539, L9

Frederick, S., Gezari, S., Graham, M. J., et al. 2019, ApJ, 883, 31

Fu, Y.M., QSOFITMORE: a python package for fitting UV-optical spectra of quasars.zenodo.5810042 doi:10.5281/zenodo.5810042

Fu, Y., Wu, X.-B., Yang, Q., et al. 2021, ApJS, 254, 6. doi:10.3847/1538-4365/abe85e

Gebhardt, K., Bender, R., Bower, G., et al. 2000, ApJL, 539, L13

Fitzpatrick, E. L. 1999, PASP, 111, 63. doi:10.1086/316293

Guo, H., Shen, Y., & Wang, S. 2018, Astrophysics Source Code Library. ascl:1809.008

Guo, H., Sun, M., Liu, X., et al. 2019, ApJL, 883, L44.

Heintz, K. E., Fynbo, J. P. U., Geier, S. J., et al. 2020, A&A, 644, A17. doi:10.1051/0004-6361/202039262

Hennawi, J. F. & Prochaska, J. X. 2007, ApJ, 655, 735. doi:10.1086/509770

Komossa, S. & Xu, D. 2007, ApJL, 667, L33. doi:10.1086/522002

Kormendy, J., & Gebhardt, K. 2001, 20th Texas Symposium on relativistic astrophysics, 586, 363

Huo, Z.-Y., Liu, X.-W., Yuan, H.-B., et al. 2010, Research in Astronomy and Astrophysics, 10, 612. doi:10.1088/1674-4527/10/7/002

Huo, Z.-Y., Liu, X.-W., Xiang, M.-S., et al. 2015, Research in Astronomy and Astrophysics, 15, 1438. doi:10.1088/1674-4527/15/8/023

Huo, Z.-Y., Liu, X.-W., Xiang, M.-S., et al. 2013, AJ, 145, 159. doi:10.1088/0004-6256/145/6/159

Jin, J.-J., Wu, X.-B., & Feng, X.-T. 2022, ApJ, 926, 184. doi:10.3847/1538-4357/ac410c

Jin, X., Zhang, Y., Zhang, J., et al. 2019, MNRAS, 485, 4539. doi:10.1093/mnras/stz680

Lawrence, A., Warren, S. J., Almaini, O., et al. 2007, MNRAS, 379, 1599. doi:10.1111/j.1365-2966.2007.12040.x

Luo, A.-L., Zhang, H.-T., Zhao, Y.-H., et al. 2012, Research in Astronomy and Astrophysics, 12, 1243. doi:10.1088/1674-4527/12/9/004

Luo, A.-L., Zhao, Y.-H., Zhao, G., et al. 2015, Research in Astronomy and Astrophysics, 15, 1095. doi:10.1088/1674-4527/15/8/002

Lyke, B. W., Higley, A. N., McLane, J. N., et al. 2020, ApJS, 250, 8. doi:10.3847/1538-4365/aba623

MacLeod, C. L., Ivezić, Ž., Sesar, B., et al. 2012, ApJ, 753, 106. doi:10.1088/0004-637X/753/2/106

MacLeod, C. L., Green, P. J., Anderson, S. F., et al. 2019, ApJ, 874, 8

Maddox, N., Hewett, P. C., Warren, S. J., et al. 2008, MNRAS, 386, 1605. doi:10.1111/j.1365-2966.2008.13138.x

Magorrian, J., Tremaine, S., Richstone, D., et al. 1998, AJ, 115, 2285

Markwardt, C. B. 2009, Astronomical Data Analysis Software and Systems XVIII, 411, 251

Merritt, D., & Ferrarese, L. 2001, MNRAS, 320, L30

Pasquet-Itam, J. & Pasquet, J. 2018, A&A, 611, A97. doi:10.1051/0004-6361/201731106

Pâris, I., Petitjean, P., Aubourg, É., et al. 2012, A&A, 548, A66. doi:10.1051/0004-6361/201220142

Pâris, I., Petitjean, P., Aubourg, É., et al. 2018, A&A, 613, A51. doi:10.1051/0004-6361/201732445

Peng, N., Zhang, Y., Zhao, Y., et al. 2012, MNRAS, 425, 2599. doi:10.1111/j.1365-2966.2012.21191.x

Rakshit, S., Stalin, C. S., & Kotilainen, J. 2020, ApJS, 249, 17. doi:10.3847/1538-4365/ab99c5

Richards, G. T., Fan, X., Newberg, H. J., et al. 2002, AJ, 123, 2945. doi:10.1086/340187

Richards, G. T., Nichol, R. C., Gray, A. G., et al. 2004, ApJS, 155, 257. doi:10.1086/425356

Richards, G. T., Lacy, M., Storrie-Lombardi, L. J., et al. 2006, ApJS, 166, 470. doi:10.1086/506525

Richards, G. T., Strauss, M. A., Fan, X., et al. 2006, AJ, 131, 2766. doi:10.1086/503559

Richards, G. T., Myers, A. D., Gray, A. G., et al. 2009, ApJS, 180, 67. doi:10.1088/0067-0049/180/1/67

Ross, N. P., Myers, A. D., Sheldon, E. S., et al. 2012, ApJS, 199, 3. doi:10.1088/0067-0049/199/1/3

Runco, J. N., Cosens, M., Bennert, V. N., et al. 2016, ApJ, 821, 33. doi:10.3847/0004-637X/821/1/33

Salviander, S., Shields, G. A., Gebhardt, K., et al. 2007, ApJ, 662, 131. doi:10.1086/513086

Schlegel, D. J., Finkbeiner, D. P., & Davis, M. 1998, ApJ, 500, 525. doi:10.1086/305772

Schmidt, M. 1963, Nature, 197, 1040. doi:10.1038/1971040a0

Schneider, D. P., Hall, P. B., Richards, G. T., et al. 2007, AJ, 134, 102. doi:10.1086/518474

Schmidt, E. O., Oio, G. A., Ferreiro, D., et al. 2018, A&A, 615, A13. doi:10.1051/0004-6361/201731557

Silverman, J. D., Green, P. J., Kim, D.-W., et al. 2002, ApJL, 569, L1. doi:10.1086/340458

Sharp, R. G., Sabbey, C. N., Vivas, A. K., et al. 2002, MNRAS, 337, 1153. doi:10.1046/j.1365-8711.2002.05961.x

Shen, Y., Richards, G. T., Strauss, M. A., et al. 2011, ApJS, 194, 45. doi:10.1088/0067-0049/194/2/45

Shin, J., Nagao, T., Woo, J.-H., et al. 2019, ApJ, 874, 22. doi:10.3847/1538-4357/ab05da

Shen, Y., Hall, P. B., Horne, K., et al. 2019, ApJS, 241, 34. doi:10.3847/1538-4365/ab074f

Smail, I., Sharp, R., Swinbank, A. M., et al. 2008, MNRAS, 389, 407. doi:10.1111/j.1365-2966.2008.13579.x

Tremaine, S., Gebhardt, K., Bender, R., et al. 2002, ApJ, 574, 740

Tsuzuki, Y., Kawara, K., Yoshii, Y., et al. 2006, ApJ, 650, 57. doi:10.1086/506376

Vanden Berk, D. E., Richards, G. T., Bauer, A., et al. 2001, AJ, 122, 549. doi:10.1086/321167

Vestergaard, M. & Wilkes, B. J. 2001, ApJS, 134, 1. doi:10.1086/320357

Vestergaard, M. & Peterson, B. M. 2006, ApJ, 641, 689. doi:10.1086/500572

Wang, J.-G., Dong, X.-B., Wang, T.-G., et al. 2009, ApJ, 707, 1334. doi:10.1088/0004-637X/707/2/1334

Wang, S., Shen, Y., Jiang, L., et al. 2019, ApJ, 882, 4. doi:10.3847/1538-4357/ab322b

Wang, J., Xu, D. W., Wang, Y., et al. 2019, ApJ, 887, 15

Warren, S. J., Hewett, P. C., & Foltz, C. B. 2000, MNRAS, 312, 827. doi:10.1046/j.1365-8711.2000.03206.x

Webb, N. A., Coriat, M., Traulsen, I., et al. 2020, A&A, 641, A136. doi:10.1051/0004-6361/201937353

Worseck, G., Wisotzki, L., & Selman, F. 2008, A&A, 487, 539. doi:10.1051/0004-6361:200810157

Wright, E. L., Eisenhardt, P. R. M., Mainzer, A. K., et al. 2010, AJ, 140, 1868. doi:10.1088/0004-6256/140/6/1868

Wu, X.-B. & Jia, Z. 2010, MNRAS, 406, 1583. doi:10.1111/j.1365-2966.2010.16807.x

Wu, X.-B., Hao, G., Jia, Z., et al. 2012, AJ, 144, 49. doi:10.1088/0004-6256/144/2/49

Xiang, M. S., Liu, X. W., Yuan, H. B., et al. 2015, MNRAS, 448, 90. doi:10.1093/mnras/stu2434

Yang, Q., Wu, X.-B., Fan, X., et al. 2018, ApJ, 862, 109

Yao, S., Wu, X.-B., Ai, Y. L., et al. 2019, ApJS, 240, 6. doi:10.3847/1538-4365/aaef88

Yèche, C., Petitjean, P., Rich, J., et al. 2010, A&A, 523, A14. doi:10.1051/0004-6361/200913508

Yuan, H., Zhang, H., Zhang, Y., et al. 2013, Astronomy and Computing, 3, 65. doi:10.1016/j.ascom.2013.12.001

Zamfir, S., Sulentic, J. W., Marziani, P., et al. 2010, MNRAS, 403, 1759. doi:10.1111/j.1365-2966.2009.16236.x

Zeimann, G. R., White, R. L., Becker, R. H., et al. 2011, ApJ, 736, 57. doi:10.1088/0004-637X/736/1/57

Zhao, G., Zhao, Y.-H., Chu, Y.-Q., et al. 2012, Research in Astronomy and Astrophysics, 12, 723. doi:10.1088/1674-4527/12/7/002